

Article

Design of Broadband Flat Optical Frequency Comb Based on Cascaded Sign-Alternated Dispersion Tellurite Microstructure Fiber

Guocheng Huang, Meicheng Fu, Junli Qi, Jinghan Pan, Wenjun Yi and Xiujuan Li *

Department of Physics, College of Liberal Arts and Sciences, National University of Defense Technology, Changsha 410073, China; hgc@nudt.edu.cn (G.H.); fumeicheng10@nudt.edu.cn (M.F.); qijunli_r@nudt.edu.cn (J.Q.); panjinghan18@nudt.edu.cn (J.P.); yiwunjun@nudt.edu.cn (W.Y.)

* Correspondence: xjli@nudt.edu.cn

Abstract: We designed a tellurite microstructure fiber (TMF) and proposed a broadband optical frequency comb generation scheme that was based on electro-optical modulation and cascaded sign-alternated dispersion TMF (CSAD-TMF). In addition, the influence of different nonlinear effects, the ultrashort pulse evolution in the CSAD-TMF with the anomalous dispersion (AD) zones and the normal dispersion (ND) zones were analyzed based on the generalized nonlinear Schrödinger equations (GNLSE) modelling. According to the simulations, when the input seed comb had a repetition rate of 20 GHz and had an input pulse peak power of 30 W, the generation scheme could generate optical frequency combs with a 6 dB spectral bandwidth spanning over 170 nm centered at 1550 nm. Furthermore, the generated combs showed good coherence in performance over the whole 6 dB spectral bandwidth. The highly coherent optical frequency combs can be used as high-repetition-rate, multi-wavelength light sources for various integrated microwave photonics and ultrafast optical signal processing applications.

Keywords: optical frequency comb; microstructure fiber; nonlinear optics; cascaded sign-alternated dispersion

Citation: Huang, G.; Fu, M.; Qi, J.; Pan, J.; Yi, W.; Li, X. Design of Broadband Flat Optical Frequency Comb Based on Cascaded Sign-Alternated Dispersion Tellurite Microstructure Fiber. *Micromachines* **2021**, *12*, 1252. <https://doi.org/10.3390/mi12101252>

Academic Editors: Minhao Pu and Jing Xu

Received: 22 September 2021

Accepted: 12 October 2021

Published: 15 October 2021

Publisher's Note: MDPI stays neutral with regard to jurisdictional claims in published maps and institutional affiliations.



Copyright: © 2021 by the authors. Licensee MDPI, Basel, Switzerland. This article is an open access article distributed under the terms and conditions of the Creative Commons Attribution (CC BY) license (<https://creativecommons.org/licenses/by/4.0/>).

1. Introduction

The optical frequency comb (OFC) refers to a series of discrete, equally spaced frequency components, which covers a variety of applications such as optical frequency metrology, laser ranging, and astronomical spectrograph calibration [1–3]. Based on various applications, several schemes have been demonstrated to generate OFCs, including a mode-locked laser [4,5], an electro-optic frequency comb [6–8], and a Kerr comb [9,10]. For the unique advantages of high repetition rates, spectral flatness, robustness, and re-configuration flexibility, the electro-optic frequency comb has received considerable attention as a valid tool for numerous RF photonic applications such as wavelength division multiplexing, optical arbitrary waveform generation, and all-optical signal processing [11–14]. The electro-optic frequency comb can be generated by various methods, including the use of a dual-drive Mach–Zehnder modulator (MZM) [15], cascading intensity modulators (IM), phase modulators (PM) [16], time-to-frequency mapping [17], and so on, in which the comb lines number and bandwidth coverage are limited by the modulator's bandwidth and the performance of the RF source.

To promote comb bandwidth, highly nonlinear mediums have been applied for nonlinear broadening. By utilizing 150 m of highly nonlinear fiber (HNLF) with normal dispersion profile, a 10 GHz ultra-broadband comb (28 nm bandwidth within 3.5 dB power variation) generator was demonstrated [16]. In 2020, based on a precise parameter mixer setup, a sub-100 fs all-fiber electro-optic OFC which had a 6 dB spectral bandwidth

spanning over 150 nm was demonstrated [8]. Recently, a non-coherent broad seed comb was generated by using a single MZM, then an OFC of 55 frequency lines with 3 dB flatness was obtained via four-wave mixing in 400 m of HNLF [18]. Another study demonstrated that, via sign-alternated dispersion, the stagnation of spectral broadening can be eliminated, and the required power can be significantly reduced [19]. However, most of the current schemes rely on silica highly nonlinear fiber (SHNLF) [6, 15, 20], in which the inherent nonlinear refractive index limits the improvement of the nonlinear coefficient ($10\sim 20 \text{ W}^{-1}\text{km}^{-1}$), and the lengthening of the SHNLF will reduce the threshold of SBS and cause the zero-dispersion wavelength to shift. Fortunately, a growing number of new materials with a higher nonlinear coefficient and broader transmission windows have been demonstrated recently [21–23]. Among them, tellurite microstructure fiber (TMF), which is based on $70\text{TeO}_2\text{-}20\text{BaF}_2\text{-}10\text{Y}_2\text{O}_3$ glasses, has a high nonlinear refractive index, stable chemical and thermal properties, high damage threshold [24], and a large transparent band ranging from the visible band to the long-wave infrared ($\approx 5 \mu\text{m}$) band. Furthermore, the nonlinearity coefficient of the TMF is at least one order of magnitude higher than that of the SHNLF [25]. All of the above unique properties of TMF reveal its great potential in supercontinuum and frequency comb generation [26, 27].

In previous work [28], a flat-top optical frequency comb covering 1500–1600 nm was generated by using a 2 m long, near-zero dispersion fluoroantimonate microstructure fiber. However, the results show that the fiber dispersion was greatly affected by the inner air hole parameter, and that it was hard to keep near-zero dispersion. Herein, we proposed an efficient scheme based on a designed cascaded sign-alternated dispersion TMF (CSAD-TMF) with cascaded normal dispersion (ND) zones and anomalous dispersion (AD) zones to overcome this limitation.

As shown in Figure 1, the schematic diagram of a broadband flat OFC generator based on the CSAD-TMF can be divided into two stages: Stage 1 and Stage 2. In Stage 1, the seed frequency comb is generated by a dual-drive MZM and a PM driven by a 20 GHz RF signal with equal phase. Here, the half-wave voltage at the DC bias voltage port and the RF drive port of the dual-drive MZM are set to 5 V and 1.6 V, respectively. The output optical signal has a positive chirp after passing through the PM, then a 290 m single-mode fiber is set for chirp elimination to perform ultra-short pulses simultaneously. The high-power erbium-doped fiber amplifier (EDFA) lifts the pulse peak power up to 30 W. In Stage 2, the generated seed comb passes through a sign-alternated dispersion TMFs with five cascaded ND and AD fiber segments with different designed lengths, which broaden the output spectrum through nonlinear effects such as four-wave mixing and self-phase modulation.

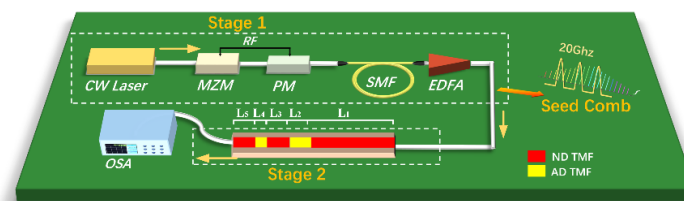


Figure 1. Schematic diagram of a broadband flat OFC generator based on CSAD-TMF.

2. Generation of Electro-Optic Seed Comb

The center wavelength of the CW laser in Stage 1 was 1550 nm with linewidth of 20 kHz, and the output power was 10 dBm. The output optical signal of the dual-drive MZM can be expressed as:

$$E_{\text{mzm}} = \frac{1}{2} E_{\text{in}} \sum_{k=-\infty}^{+\infty} [J_k(\alpha_1) e^{i(\omega t - \Delta\phi)} + J_k(\alpha_2) e^{i(\omega t + \Delta\phi)}], \quad (1)$$

where E_{in} is the amplitude of the input RF signal with frequency of ω , J_k is the k -order Bessel function, and $\alpha_i = \pi \frac{V_i}{V_{\pi,RF}}$ ($i = 1, 2$) represents the modulation index of two input RF signals. $\Delta\phi = \pi \frac{\Delta V_{DC}}{V_{\pi,DC}}$ represents the phase difference introduced by two DC bias ports, in which the DC bias voltage difference ΔV_{DC} is set to 3 V for the following analysis. According to the measurements, the driving voltages V_1 and V_2 were set to 6 V and 4.65 V for the simulation, respectively. Under the above conditions, a flat OFC with 11 comb lines with 2.3 dB flatness can be observed in Figure 2a. After the phase modulator, the signal can be expressed as:

$$E_{out} = E_{mzm} \sum_{k=-\infty}^{+\infty} J_k(\alpha_3) e^{ik\omega t}, \quad (2)$$

where $\alpha_3 = \pi \frac{V_3}{V_{\pi,PM}}$ is the phase deviation of the phase modulator, and $V_{\pi,PM}$ is the corresponding half-wave voltage. When the phase deviation was set to 5π , 21 comb lines with 2.4 dB flatness was obtained, as shown in Figure 2b,c. Then, after the 290 m single-mode fiber that followed the phase modulator, which was used for chirp elimination, the compressed shortest pulse was obtained, wherein FWHM was ~ 1 ps, as shown in Figure 2d, in which the dotted line gives the chirp of the pulse. The chirp of the main pulse was completely eliminated after compression, but there were still some low power sidelobes in the time domain, which may have affected the spectral flatness of the OFC after Stage 2.

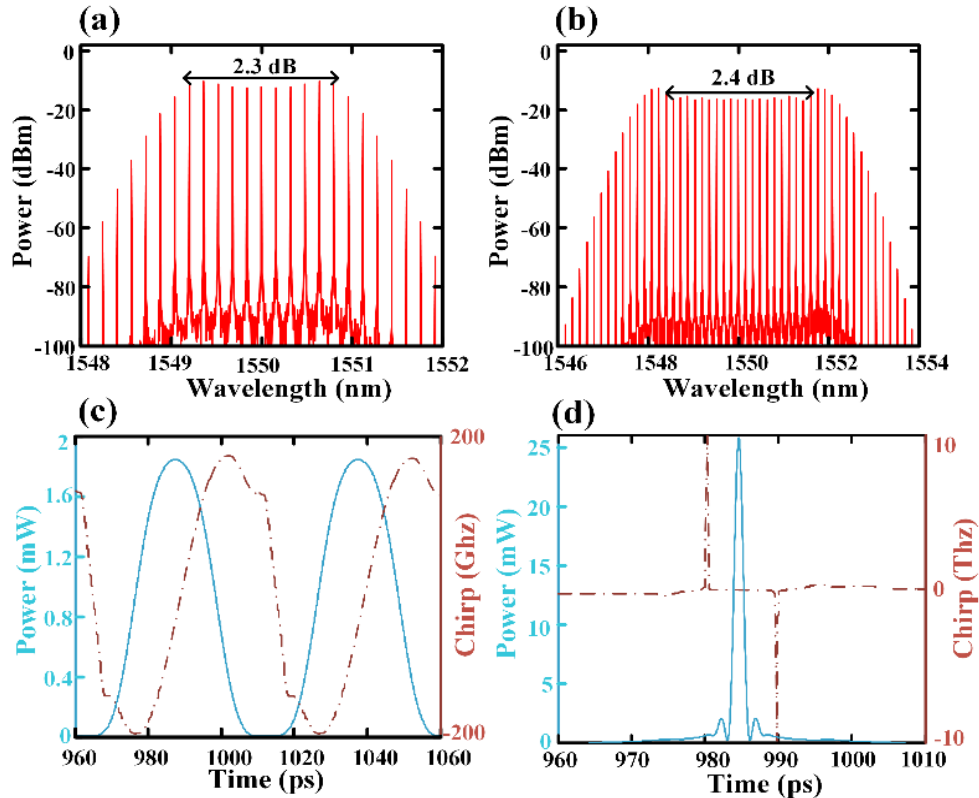


Figure 2. (a) The spectrum of OFC generated by a single MZM; (b) the spectrum of OFC generated by cascaded dual-drive MZM and phase modulator; (c) the time domain of the pulse after phase modulator; (d) the time domain and chirp of the pulse after the compression of single-mode fiber.

3. Design and Optimization of CSAD-TMF

To achieve a flat OFC, the sign-alternated dispersion TMF in Stage 2 was finely designed. As shown in Figure 3a, the TMF core is surrounded by two layers of regular hexagonal air holes. The diameter of the outer air holes is D_1 and the hole spacing is Λ , while the diameter of the inner air holes is D_2 and the hole spacing is k , which can be finely tuned to adjust the dispersion of the TMF effectively.

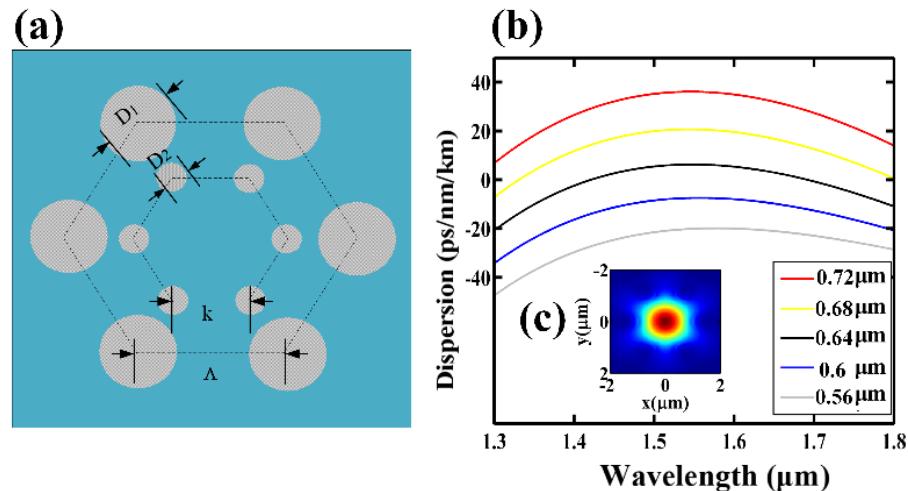


Figure 3. (a) Cross-section of the TMF; (b) the dispersion of the TMF when D_2 changes from 0.56 μm to 0.72 μm for $k = 1.27 \mu\text{m}$; (c) the field profiles of the fundamental modes in TMF.

To achieve a zero dispersion wavelength of 1550 nm, D_1 was set to 3.8 μm and Λ was set to 4 μm according to the dispersion regulation in [28]. Furthermore, the inner holes can be finely adjusted for obtaining a flatter normal dispersion and anomalous dispersion profile over the C-band. The inner hole spacing k was optimally set to 1.27 μm . The inner holes diameter D_2 was further finely adjusted. It was found that when D_2 was increased from 0.56 μm to 0.72 μm , the dispersion at 1550 nm would transform from the ND to the AD with nearly the same dispersion slope, as shown in Figure 3b. Figure 3c shows the field distribution of the fundamental transverse electric mode (TE) at the cross section of the TMF for $D_2 = 0.6 \mu\text{m}$. Most of the energy was concentrated in the core of the TMF with the effective mode field area $A_{\text{eff}} = 2.11 \mu\text{m}^2$. The calculated nonlinear coefficient is given by $\gamma = \frac{2\pi n_2}{\lambda A_{\text{eff}}}$, where n_2 is the nonlinear refractive index and λ is the working wave-

length. According to the above analysis, we selected $D_2 = 0.6 \mu\text{m}$ for the ND zone and $D_2 = 0.72 \mu\text{m}$ for the AD zone. The main simulation parameters, including the second order dispersion, the third order dispersion, effective field areas, nonlinear coefficients of the TE modes, and the transmission loss, are listed in Table 1.

Table 1. Some of the main simulation parameters of ND TMF and AD TMF.

Zone	D_2 (μm)	β_2 (ps^2/km)	β_3 (ps^3/km)	A_{eff} (μm^2)	γ ($\text{m}^{-1}\text{W}^{-1}$)	Loss (dB/m)
ND TMF	0.6	9.4601	−0.0085	2.55	2.2255	1.5
AD TMF	0.72	−45.9939	0.0703	2.11	2.6896	1.5

4. Numerical Simulations

To analyze the pulse evolution in the CSAD-TMF, numerical simulations were performed by solving the generalized nonlinear Schrödinger equations (GNLSE). Firstly, the transmission characteristics of an unchirped hyperbolic secant pulse in the designed TMF

were analyzed. The FWHM of the input pulse was 1 ps, its center wavelength was 1550 nm and peak power was 30 W. In the simulation, the dispersion above the fourth order was ignored, and the fourth order Runge–Kutta algorithm was used to reduce the iterative error. Figure 4a,b show the evolution of the single pulse transmitting through a 2.5 m ND TMF. When the compressed pulse passes through the ND zone, owing to the SPM and optical wave breaking (OWB) [29,30], the pulse will continuously expand in the time domain and the frequency domain with increasing transmission distance up to a certain value. This leads to the formation of a flat frequency domain envelope, as shown in Figure 4a. When the transmission length is less than 2 m, the spectrum of the pulse continues to be widened with the increase of the transmission length, and the broadening in the blue shift and the red shift directions are roughly symmetrical. When the transmission distance is between 2 m and 2.5 m, the spectrum broadening has basically ended.

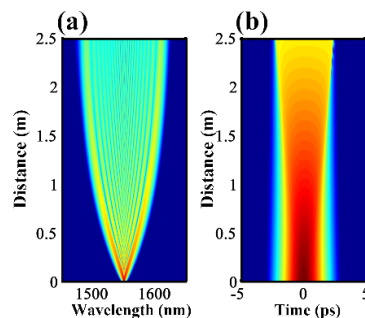


Figure 4. (a,b) Evolution of pulses and spectrum in a 2.5m ND TMF.

In the ND zone, the maximum spectrum width of the generated OFC and the splitting distance can be estimated by the following empirical formula:

$$|f_{SPM}(L_{OWB}) - f_0|_{max} \propto (\gamma P_0 / |\beta_2|)^{1/2}, \quad (3)$$

$$L_{OWB} \propto T_0 \sqrt{1 / \gamma P_0 |\beta_2|}, \quad (4)$$

where f_{SPM} is the maximum value of spectrum broadening contributed by the SPM, and f_0 is the center frequency of the pulse. It can be observed from Equation (3) that, in the ND region, the spectrum broadening width depends on the nonlinear coefficient, the GVD value, the pulse width, the peak power of the input pulse, and the transmission distance required for the spectrum envelope flattening by the OWB.

Theoretically, larger spectrum broadening can be obtained by appropriately increasing the input power and reducing the pulse width. However, it is difficult to obtain high-power short pulses and the tolerance of the material itself is also limited. High energy consumption is also not conducive to system integration. Here, we use CSAD-TMF to optimize the pulse evolution and the spectrum broadening.

The evolution results of the same pulse in the CSAD-TMF are given in Figure 5. The length of the ND TMF and the AD TMF were determined as 0.7 m and 0.2 m, respectively, after optimization. The ND zone and AD zone can be connected by a tapering process [31], and the connection loss is ignored. In the 0.7 m ND zone, the pulse was broadened in both the time domain and the frequency domain, and the peak power of the pulse decreased simultaneously, as shown in Figure 5a,b. However, the flat top pulse envelope did not appear because of the short transmission distance. Then, the AD TMF was introduced to compress the pulse width and promote the peak power. In the AD zone, soliton compression occurs due to anomalous dispersion and SPM. The soliton order N is defined as follows:

$$N = \sqrt[2]{\frac{L_D}{L_{NL}}} = \sqrt[2]{\frac{Y P_0 T_0^2}{|\beta_2|}}, \quad (5)$$

where $L_D = T_0^2 / |\beta_2|$ is the dispersion length, which depends on the input pulse width T_0 , and the group velocity dispersion value of β_2 . $L_{NL} = 1 / \gamma P_0$ is the nonlinear length and is decided by the nonlinear coefficient γ and the peak input power P_0 .

For $N = 1$, i.e., the fundamental soliton, the group velocity dispersion (GVD) effect and the self-phase modulation (SPM) effect were balanced, where the shape and the spectrum of the pulse remained unchanged. For $N \geq 2$, i.e., the higher-order soliton, the SPM played the major role at the beginning, which caused a red shift on the leading edge and a blue shift on the trailing edge of the pulse. In the AD zone, the transmission speed difference between the red spectral components and the blue spectral components resulted in the compression of the pulse and the broadening of the spectrum, as shown in Figure 5c,d. However, when broadening of the spectrum happens, the dispersion will become dominant and even soliton splitting will occur. When the transmission distance exceeds 0.25 m, soliton fission occurs and the flatness of the output comb is destroyed. Therefore, the length of the AD zone was set to 0.2 m.

The spectrograms of the output pulse after the ND zone and the AD zone were calculated using the XFROG technique, as shown in Figure 5e,g. The spectrogram of the initial pulse is given in Figure 5e. In the ND zone, the red spectral components travelled faster and became the leading edge of the pulse, which combined with the center wavelength component to produce new frequency components. A similar phenomenon can also be observed at the trailing edge of the pulse. As a result, some of the energy at the center wavelength of the pulse shifted to both ends of the spectrum continuously, which can be observed in Figure 5f.

In the AD zone, the pulse evolution is mainly determined by the soliton compression, in which the compression of the pulse leads to energy concentration and broadening of the spectrum. After the transmission in the CSAD-TMF (0.7 m ND TMF and 0.2 m AD TMF), the spectrum was broadened by more than 100 nm, as shown in Figure 5c,g. In future research, more sign-alternated subintervals will be added for further optimization.

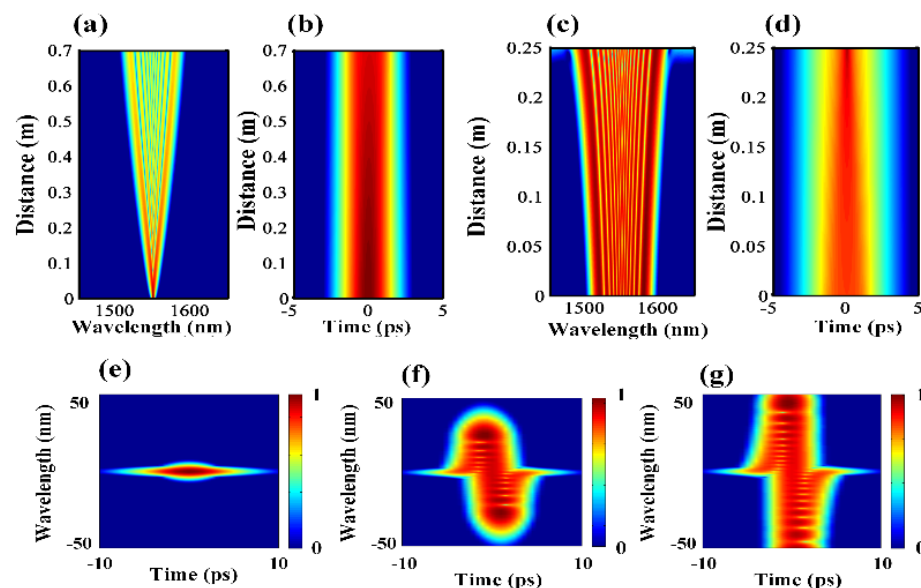


Figure 5. (a,b) Evolution of the pulses and the spectrum in 0.7 m ND TMF; (c,d) evolution of the pulses and the spectrum in 0.2 m TMF; (e) the initial pulse trace; (f) the pulse trace after the ND zone; (g) the pulse trace after the AD zone.

The evolution of a single pulse in the ND TMF and the optimized CSAD-TMF is discussed below. Figure 6a,b show the pulse evolutions when the length of the ND TMF is 0.5 m, 1 m, 1.5 m, 2 m, and 2.5 m, respectively. In the time domain, the linear positive chirp provided by the normal dispersion broadened and reshaped the pulse into a rectangular pulse with an approximate flat top, while the leading anti-trailing edges became steeper. The corresponding spectrum was widened to cover 1500–1600 nm, and then the flatness was gradually improved when the transmission length exceeded 2 m. Finally, a flat optical frequency comb in the range of 1500–1600 nm was obtained.

For the CSAD-TMF, the length of each segment is $L_1 = 0.7$ m (ND), $L_2 = 0.2$ m (AD), $L_3 = 0.3$ m (ND), $L_4 = 0.05$ m, and $L_5 = 0.3$ m, respectively, as shown in Figure 1. In Figure 6c,d, L_n ($n = 1, 2, 3, 4, 5$) in the figure represents the output result when passing the n th segment in the CSAD-TMF. According to the pulse evolutions and spectrum shown in Figure 6c,d, the AD zones L_2 and L_4 compressed the pulse, but the corresponding spectrum broadening was not obvious. After the ND zone L_1 , the spectrum covered 1520–1580 nm, while after the ND zone L_3 , the spectrum was broadened and covered 1480–1610 nm, which was 70 nm wider than the spectrum after the ND zone L_1 . For the ND zone L_5 , the spectrum broadening was only about 10 nm more than the ND zone L_3 , but the flatness was significantly improved. Finally, a flat optical frequency comb with a spectral range of 1460–1650 nm was obtained.

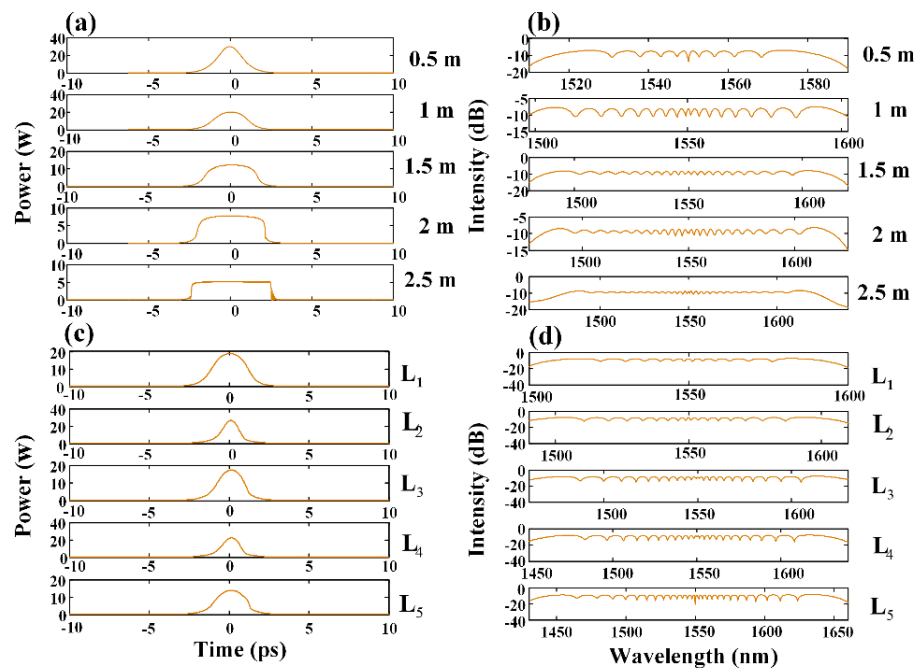


Figure 6. (a,b) Evolution of pulses at different positions of 2.5 m ND TMF; (c,d) Evolution of single pulse after different ND and AD zones of optimized CSAD-TMF.

Besides the spectral width and flatness, the coherence is another significant criterion to evaluate the performance of OFC, especially for applications such as super-high-capacity optical transmission based on WDM and TDM. Noise effects can be rigorously analyzed through the inclusion of stochastic variables to characterize quantum-limited shot noise [32]. Theoretically, the coherence of the OFC can be calculated by:

$$|g_{12}(\lambda)| = \frac{\left| \langle |E_1(\lambda)|^2 |E_2(\lambda)|^2 \rangle \right|}{\left[\langle |E_1(\lambda)|^2 \rangle \langle |E_2(\lambda)|^2 \rangle \right]^{1/2}}, \quad (6)$$

where the angular brackets denote an ensemble average over independently generated pairs of OFC spectra and $\langle (E_1(\lambda), E_2(\lambda)) \cdot |g_{12}(\lambda)| = 1$ represents the full coherence of the OFC.

Figure 7 shows the calculation results of OFC coherence at the different transmission stages of CSAD-TMF. In the output of the AD zone L_1 , the coherence in the range of 1450–1650 nm was close to 1, as shown in Figure 7. At the end of AD zone L_2 , the coherence degraded, even dropping to below 0.9 at 1510 nm and 1535 nm, as a result of the modulation instability in the AD zone, which amplified both the coherent frequency component and the random noise. The AD zone TMF will degenerate the coherence of the OFC, while the ND zone TMF will make the distribution of coherence over the whole spectral band more consistent. It can be seen that in the output of the CSAD-TMF, the OFC coherence remained mostly above 0.9 in the range of 1450–1650 nm, which indicated that the OFC produced by this scheme had good coherence, and the phase relationship between different frequency components was stable.

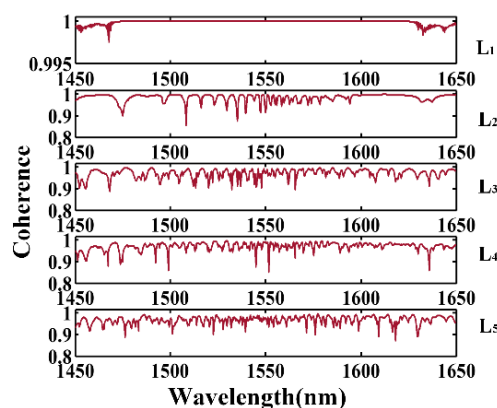


Figure 7. The coherence of the generated OFC from 1450 nm to 1650 nm after different ND and AD zones of optimized CSAD-TMF.

The evolution of a seed electro-optic OFC with a repetition rate of 20 GHz in the designed CSAD-TMF is demonstrated in Figure 8. After the transmission distance L_1 , spectrum broadening occurred between 1550 and 1600 nm because of SPM, OWB, and a cascaded four-wave mixing (FWM) effect in the ND zone, while the peak power of the pulse was attenuated from 30 W to approximately 18 W. After the transmission distance L_2 in the AD zone, the peak power of the pulse increased to approximately 25 W while the pulse width compressed. As a result of the cascaded pulse compression, dispersion compensation, and broadening in the AD zones and in the ND zones, at the output of the ND zone L_5 , a flat top optical frequency comb covering 1460–1660 nm was obtained. An enlarged image of the final output spectrum between 1560 nm and 1660 nm is given in Figure 8c. It can be observed that the flatness of the generated OFC was about 6 dB over the range of 1565–1650 nm. Due to the spectral symmetry on both sides of the central wavelength, the final output spectrum of the OFC at the output of the CSAD-TMF had a 6 dB bandwidth of 170 nm.

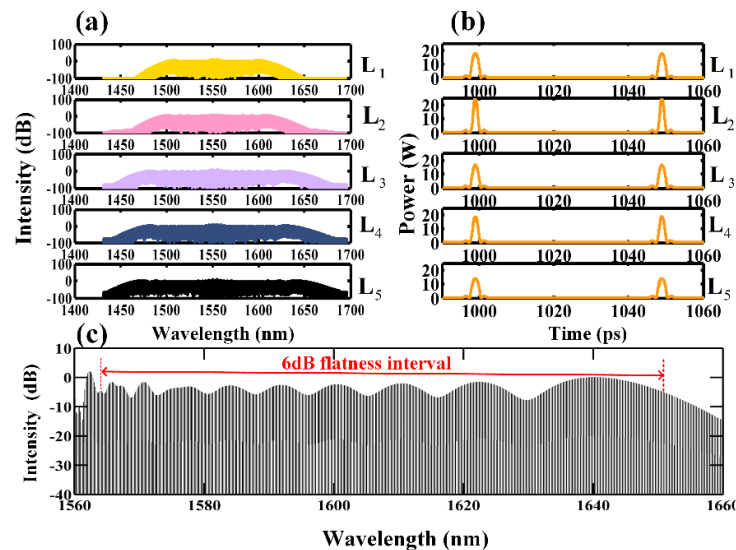


Figure 8. (a) The output spectra at different stages of CSAD-TMF; (b) the evolution of pulse profiles at different stages of CSAD-TMF; (c) the enlarged image of the final output spectrum over 1560–1660 nm.

5. Conclusions

In summary, a scheme based on the designed CSAD-TMF was proposed for generating broadband OFC. In the modelling of the TMF, we considered a geometry with two layers of regular hexagonal air holes, and the dispersion characteristics of the cross-section were calculated to achieve optimized design parameters. By considering the influence of different nonlinear effects, the ultrashort pulse evolution in the AD zone and ND zone of the CSAD-TMF was analyzed based on GNLSE. Then, by injecting a 20 GHz high-repetition-rate seed OFC into the optimized CSAD-TMF, the output spectra after passing through different TMF zones were demonstrated, and highly coherent combs with a 6 dB width covering over 170 nm were obtained. The OFC generator based on the optimized CSAD-TMF can effectively break through the bandwidth limit of electro-optic modulation, which will be useful for exploring high-repetition-rate, multi-wavelength light sources for various integrated microwave photonics and ultrafast optical signal processing applications.

Author Contributions: Conceptualization, X.L. and G.H.; methodology, G.H.; software, M.F.; validation, G.H. and W.Y.; formal analysis, J.Q. and G.H.; investigation, M.F. and J.P.; data curation, G.H.; writing, all authors; supervision, X.L. All authors have read and agreed to the published version of the manuscript.

Funding: This research was funded by the National Science Foundation of China (NSFC) (60673147, 61070040, 61205087, 61107005, 62005317, 62005207), Hunan Provincial Natural Science Foundation of China (805297133191), Natural Science Foundation of Shaanxi Province (2019JQ-648), and The National Key Research and Development Program of China (NKRDPC) No. 2020YFA0713504.

Conflicts of Interest: The authors declare no conflict of interest.

References

1. Jones, D.J.; Diddams, S.A.; Ranka, J.K.; Stentz, A.; Windeler, R.S.; Hall, J.L.; Cundiff, S.T. Carrier-envelope phase control of femtosecond Mode-Locked lasers and direct optical frequency synthesis. *Science* **2000**, *288*, 635.
2. Coddington, I.; Swann, W.C.; Nenadovic, L.; Newbury, N.R. Rapid and precise absolute distance measurements at long range. *Nat. Photonics* **2009**, *3*, 351–356.
3. Steinmetz, T.; Wilken, T.; Araujo-Hauck, C.; Holzwarth, R.; Hänsch, T.W.; Pasquini, L.; Manescau, A.; D’Odorico, S.; Murphy, M.T.; Kentischer, T.; et al. Laser frequency combs for astronomical observations. *Science* **2008**, *321*, 1335.

4. Jang, H.; Kim, B.S.; Chun, B.J.; Kang, H.J.; Jang, Y.; Kim, Y.W.; Kim, Y.; Kim, S. Comb-rooted multi-channel synthesis of ultra-narrow optical frequencies of few Hz linewidth. *Sci. Rep.* **2019**, *9*, 7652.
5. Akamatsu, D.; Inaba, H.; Hosaka, K.; Yasuda, M.; Onae, A.; Suzuyama, T.; Amemiya, M.; Hong, L. Spectroscopy and frequency measurement of the 87Sr clock transition by laser linewidth transfer using an optical frequency comb. *Appl. Phys. Express (APEX)* **2014**, *7*, 12401.
6. Kashiwagi, K.; Kurokawa, T.; Okuyama, Y.; Mori, T.; Tanaka, Y.; Yamamoto, Y.; Hirano, M. Direct generation of 12.5-GHz-spaced optical frequency comb with ultrabroad coverage in near-infrared region by cascaded fiber configuration. *Opt. Express* **2016**, *24*, 8120–8131.
7. Qu, K.; Zhao, S.; Li, X.; Zhu, Z.H.; Liang, D. Ultra-Flat and broadband optical frequency comb generator via a single mach-zehnder modulator. *IEEE Photonics Technol. Lett.* **2016**, *29*, 255–258.
8. Zhang, X.; Zhang, J.; Yin, K.; Li, Y.; Zheng, X.; Jiang, T. Sub-100 fs all-fiber broadband electro-optic optical frequency comb at 1.5 μm . *Opt. Express* **2020**, *28*, 34761–34771.
9. Grudinin, I.S.; Huet, V.; Yu, N.; Matsko, A.B.; Gorodetsky, M.L.; Maleki, L. High-contrast Kerr frequency combs. *Optica* **2017**, *4*, 434–437.
10. Fu, M.; Zheng, Y.; Li, G.; Hu, H.; Pu, M.; Oxenløwe, L.K.; Frandsen, L.H.; Li, X.; Guan, X. High-Q titanium dioxide micro-ring resonators for integrated nonlinear photonics. *Opt. Express* **2020**, *28*, 39084–39092.
11. Tang, Z.; Li, Y.; Yao, J.; Pan, S. Photonics-based microwave frequency mixing: Methodology and applications. *Laser Photonics Rev.* **2020**, *14*, 1800350.
12. Jiang, Z.; Huang, C.; Leaird, D.E.; Weiner, A.M. Optical arbitrary waveform processing of more than 100 spectral comb lines. *Nat. Photonics* **2007**, *1*, 463–467.
13. Lukens, J.M.; Lu, H.H.; Qi, B.; Lougovski, P.; Weiner, A.M.; Williams, B.P. All-optical frequency processor for networking applications. *J. Lightwave Technol.* **2020**, *38*, 1678–1687.
14. Xu, B.; Fan, X.; Wang, S.; He, Z. Wideband and high-resolution spectroscopy based on an ultra-fine electro-optic frequency comb with seed lightwave selection via injection locking. *Opt. Lett.* **2021**, *46*, 1876–1879.
15. Sakamoto, T.; Kawanishi, T.; Izutsu, M. Asymptotic formalism for ultraflat optical frequency comb generation using a Mach-Zehnder modulator. *Opt. Lett.* **2007**, *32*, 1515–1517.
16. Wu, R.; Torres-Company, V.; Leaird, D.E.; Weiner, A.M. Supercontinuum-based 10-GHz flat-topped optical frequency comb generation. *Opt. Express* **2013**, *21*, 6045–6052.
17. Torres-Company, V.; Lancis, J.; Andrés, P. Lossless equalization of frequency combs. *Opt. Lett.* **2008**, *33*, 1822–1824.
18. Sharma, V.; Singh, S.; Anashkina, E.A.; Andrianov, A.V. Demonstration of optical frequency comb generation using four-wave mixing in highly nonlinear fiber. *Optik* **2021**, *241*, 166948.
19. Zia, H.; Lüpken, N.M.; Hellwig, T.; Fallnich, C.; Boller, K. Supercontinuum generation in media with sign-alternated dispersion. *Laser Photonics Rev.* **2020**, *14*, 2000031.
20. Yang, T.; Dong, J.; Liao, S.; Huang, D.; Zhang, X. Comparison analysis of optical frequency comb generation with nonlinear effects in highly nonlinear fibers. *Opt. Express* **2013**, *21*, 8508–8520.
21. Jiang, X.; Joly, N.Y.; Finger, M.A.; Babic, F.; Wong, G.K.L.; Travers, J.C.; Russell, P.S.J. Deep-ultraviolet to mid-infrared supercontinuum generated in solid-core ZBLAN photonic crystal fibre. *Nat. Photonics* **2015**, *9*, 133–139.
22. Cheng, T.; Nagasaka, K.; Tuan, T.H.; Xue, X.; Matsumoto, M.; Tezuka, H.; Suzuki, T.; Ohishi, Y. Mid-infrared supercontinuum generation spanning 2.0 to 15.1 μm in a chalcogenide step-index fiber. *Opt. Lett.* **2016**, *41*, 2117–2120.
23. Jin, L.; Yamanaka, M.; Sonnenschein, V.; Tomita, H.; Iguchi, T.; Sato, A.; Oh-Hara, T.; Nishizawa, N. Highly coherent tunable mid-infrared frequency comb pumped by supercontinuum at 1 μm . *Appl. Phys. Express* **2016**, *10*, 12503.
24. Liao, M.; Duan, Z.; Gao, W.; Yan, X.; Suzuki, T.; Ohishi, Y. Dispersion engineering of tellurite holey fiber with holes formed by two glasses for highly nonlinear applications. *Appl. Phys. B Lasers Opt.* **2011**, *105*, 681–684.
25. Klimczak, M.; Michalik, D.; Stepniowski, G.; Karpate, T.; Cimek, J.; Forestier, X.; Kasztelan, R.; Pysz, D.; Stępień, R.; Buczyński, R. Coherent supercontinuum generation in tellurite glass regular lattice photonic crystal fibers. *J. Opt. Soc. Am. B* **2019**, *36*, A112–A124.
26. Jia, Z.; Yao, C.; Jia, S.; Wang, F.; Wang, S.; Zhao, Z.; Qin, G.; Ohishi, Y.; Qin, W. 4.5 W supercontinuum generation from 1017 to 3438 nm in an all-solid fluorotellurite fiber. *Appl. Phys. Lett.* **2017**, *110*, 261106.
27. Huang, C.; Liao, M.; Bi, W.; Li, X.; Hu, L.; Zhang, L.; Wang, L.; Qin, G.; Xue, T.; Chen, D.; et al. Ultraflat, broadband, and highly coherent supercontinuum generation in all-solid microstructured optical fibers with all-normal dispersion. *Photonics Res.* **2018**, *6*, 601–608.
28. Li, Q.; Huang, Y.; Jia, Z.; Yao, C.; Qin, G.; Ohishi, Y.; Qin, W. Design of fluorotellurite microstructured fibers with near-zero-flattened dispersion profiles for Optical-Frequency comb generation. *J. Lightwave Technol.* **2018**, *36*, 2211–2215.
29. Liu, Y.; Tu, H.; Boppart, S.A. Wave-breaking-extended fiber supercontinuum generation for high compression ratio transform-limited pulse compression. *Opt. Lett.* **2012**, *37*, 2172–2174.
30. Tomlinson, W.J.; Stolen, R.H.; Johnson, A.M. Optical wave breaking of pulses in nonlinear optical fibers. *Opt. Lett.* **1985**, *10*, 457–459.
31. Al-Kadry, A.; Amraoui, M.E.; Messaddeq, Y.; Rochette, M. Two octaves mid-infrared supercontinuum generation in As_2Se_3 microwires. *Opt. Express* **2014**, *22*, 31131–31137.
32. Genty, G.; Coen, S.; Dudley, J.M. Supercontinuum generation in photonic crystal fiber. *Rev. Mod. Phys.* **2006**, *78*, 1135–1184.